Medical Engineering & Physics 36 (2014) 1626–1635

Contents lists available at ScienceDirect

Medical Engineering & Physics

journal homepage: www.elsevier.com/locate/medengphy

Image-based vs. mesh-based statistical appearance models of the human femur: Implications for finite element simulations

Serena Bonaretti[a,*], Christof Seiler[a,b,1], Christelle Boichon[c], Mauricio Reyes[a], Philippe Büchler[a]

[a] Institute for Surgical Technology and Biomechanics, University of Bern, Bern, Switzerland
[b] Asclepios Research Group, INRIA, Sophia Antipolis, France
[c] Ansys, Villeurbanne, France

ARTICLE INFO

Article history:
Received 2 November 2013
Received in revised form 1 September 2014
Accepted 7 September 2014

Keywords:
Statistical appearance model
Image registration
Mesh morphing
Finite element simulations
Femur mechanics

ABSTRACT

Statistical appearance models have recently been introduced in bone mechanics to investigate bone geometry and mechanical properties in population studies. The establishment of accurate anatomical correspondences is a critical aspect for the construction of reliable models. Depending on the representation of a bone as an image or a mesh, correspondences are detected using image registration or mesh morphing. The objective of this study was to compare image-based and mesh-based statistical appearance models of the femur for finite element (FE) simulations. To this aim, (i) we compared correspondence detection methods on bone surface and in bone volume; (ii) we created an image-based and a mesh-based statistical appearance models from 130 images, which we validated using compactness, representation and generalization, and we analyzed the FE results on 50 recreated bones vs. original bones; (iii) we created 1000 new instances, and we compared the quality of the FE meshes. Results showed that the image-based approach was more accurate in volume correspondence detection and quality of FE meshes, whereas the mesh-based approach was more accurate for surface correspondence detection and model compactness. Based on our results, we recommend the use of image-based statistical appearance models for FE simulations of the femur.

Published by Elsevier Ltd on behalf of IPEM.

1. Introduction

Statistical shape models provide a compact and efficient description of shape variability within a dataset. They were introduced by Cootes and Taylor in 1995 [1], and since then, they have gained remarkable popularity. In the medical image analysis field, statistical shape models have been used to study shapes of human anatomy [2–6] and morphological changes due to various pathologies and trauma [7–9]. Moreover, these models have been applied to image segmentation [1,10,11], 2D/3D reconstruction [12–15] and prediction of anatomical shapes from sparse data [16–20]. The statistical core of shape models is principal component analysis (PCA) [21], which is calculated on corresponding landmarks derived from the dataset objects. The outputs of the model are parameters and modes of variation, which can be used to investigate the variability around the mean within a dataset and to create new plausible instances [1].

Statistical appearance models represent a natural extension of statistical shape models, as they describe the variability of shapes combined with image intensities [22]. This combination is particularly relevant in bone mechanics, where computed tomography (CT) intensities are related to bone mechanical properties [23–25]. In calibrated CT images, intensities correspond to bone mineral density [26], which in turn relates to the Young's modulus through empirical relationships [25]. Bone geometry and material properties can be extracted from CT images and used for finite element (FE) simulations to assess bone quality and strength [23,27]. Commonly, FE simulations are performed on a small amount of samples due to the difficulty in retrieving data and in creating FE models, thereby limiting the generalization of findings to larger populations. Whereas a fast creation of FE models could be achieved with technical development, the collection of large homogeneous datasets is still challenging. Statistical appearance models represent a possible solution as they allow the creation of

* Corresponding author. Present address: Department of Radiology and Biomedical Imaging, University of California San Francisco, 185 Berry St, Lobby 6, Suite 350 94107 San Francisco, CA, USA. Tel.: +1 (415) 353 4923.
E-mail address: serena.bonaretti@ucsf.edu (S. Bonaretti).
[1] Present address: Department of Statistics, Stanford University, Stanford, CA, USA.

http://dx.doi.org/10.1016/j.medengphy.2014.09.006
1350-4533/Published by Elsevier Ltd on behalf of IPEM.

realistic instances, suitable for population-based studies. Moreover, the parametric description of the instances allows statistical control on shape and material property variations. For these reasons, statistical appearance models have recently been combined with FE simulations to predict bone strength [28,29] and fracture risk [9,30].

The most challenging requirement for the creation of statistical models is to establish accurate correspondences among similar features of dataset objects. For statistical appearance models, correspondences have to be accurate, not only on the surface but also in the volume. Two different approaches have been proposed for the creation of bone models, based on different representations of bone: image-based and mesh-based. In image-based approaches, bones are represented as volumetric images [9,28,31], thus voxels contain information of both shape and intensity. Correspondences among images are detected using image registration algorithms, like free-form deformation [32] and demons [33]. In the mesh-based approach, bones are represented as volumetric meshes [7,29], therefore mesh nodes contain information of shape and the intensities are associated with each node. Correspondences among meshes are established using mesh morphing techniques [30,34,35]. Both approaches have advantages and drawbacks. In the image-based approach, registration allows dense anatomical correspondence among the dataset objects. However, new instances can be generated only with invertible deformation vector fields, and they have to be meshed individually, creating difficulties when comparing mechanical results. In the mesh-based approach, morphing provides FE meshes that are directly suitable for FE calculations and that have corresponding elements. However, the variation of node positions to guarantee valid mesh elements could limit the accuracy of correspondences.

In this study, we aim to compare statistical appearance models created with one image-based and one mesh-based approach and to evaluate their implications for finite element simulations. We compare (i) the performances of two approaches for correspondence detection algorithms, image registration and mesh morphing; (ii) the quality of statistical appearance models created with the two approaches and their implications for FE results obtained from reconstructed bones vs. original bones; (iii) the quality of the FE meshes created for new instances.

2. Materials and methods

2.1. Subject data

A total of 155 left femur CT images were used in this study. Among the subjects, 70 were male and 85 female (age = 62 ± 16 years, height = 166 ± 7 cm, weight = 71 ± 16 kg), 124 were Caucasian, 28 were Asian and 3 were African. The resolution of the CT images was between 0.61×0.61 mm and 1.17×1.17 mm, with a slice thickness of 1 mm. Data acquisition was fully anonymized and controlled by a governmental data protection agency (DatenschutzbeauftragterStadt Bremen, Bremen, Germany).

From the 155 images, we randomly selected 130 images to calculate the statistical appearance models, and we used the remaining 25 images to validate the model.

2.2. Creation of statistical appearance models

We computed two statistical appearance models: one image-based and one mesh-based. For the image-based case, we considered bones as volumetric images, and we constructed the model using image voxels. For the mesh-based case, we considered bones as volumetric meshes, and we computed the model using mesh node positions and corresponding intensities at the nodes. We implemented the two approaches following the scheme depicted in Fig. 1. For both the image-based and the mesh-based approaches, we established bone anatomical correspondences (Step 1), built a statistical appearance model (Step 2) and created new instances (Step 3). For each step, we validated and compared the performances of the two approaches. We performed all computation using VTK 5.6.1 (Visualization Toolkit, Kitware), ITK 3.20.0

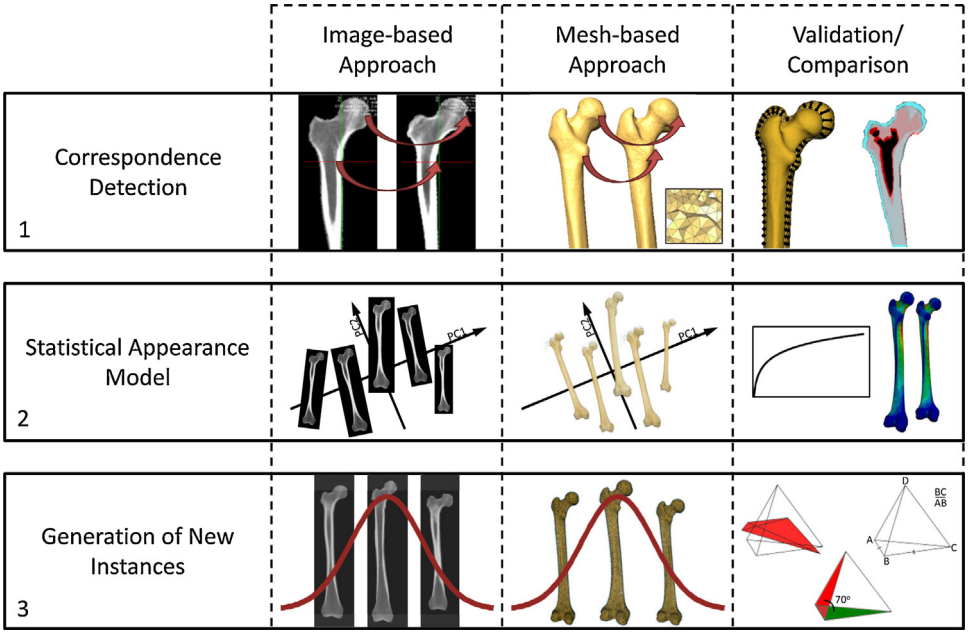

Fig. 1. Creation and evaluation of statistical appearance models using an image-based and a mesh-based approach. The models were created in three steps. Step 1 is the detection of corresponding anatomical landmarks, Step 2 is the creation of the statistical appearance models, and Step 3 is the generation of new instances. For each step, we validated the model, and for the last two steps, we compared the FE performances. For Step 1, we evaluated the accuracy of the correspondences on the bone surface using the Hausdorff distance and in the bone volume using overlapping metrics. For Step 2, we validated the models using compactness, representation and generalization, and we evaluated the FE results on the original bone vs. reconstructed bones. For Step 3, we evaluated the quality of the created meshes using Jacobian, edge ratio and minimum angle.

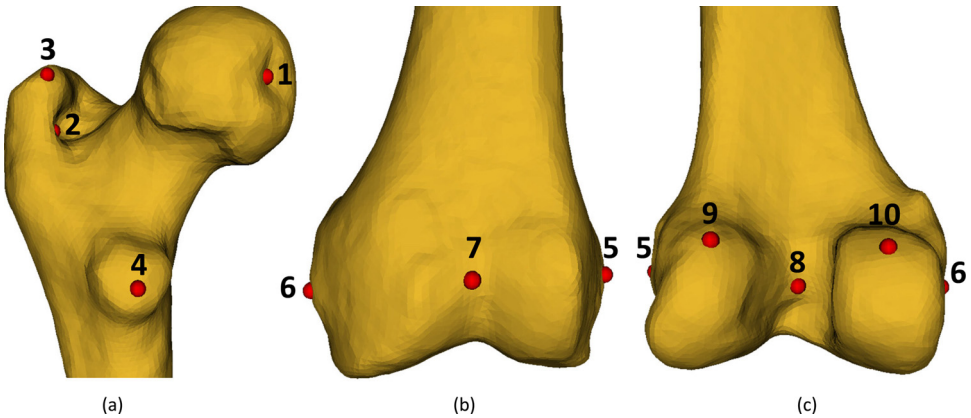

Fig. 2. Landmarks for the mesh morphing selected in (a) femoral head (1 = fovea; 2 = posterior lateral femoral neck: 3 = greater trochanter; 4 = lesser trochanter), and in (b) anterior and (c) posterior femoral condyles (5 = lateral epicondyle; 6 = medial epicondyle; 7 = patellar surface of femur; 8 = intercondyle; 9 = lateral condyle; 10 = medial condyle).

(Insight Toolkit, Kitware) and Matlab 2012 (Matlab, Natick, MA, USA).

2.2.1. Image preprocessing

For both image- and mesh-based models, we segmented the femurs semi-automatically on the original CT images using Amira (Amira 4, Visage Imaging Inc., USA). For each femur, we labeled cortical bone, cancellous bone and bone marrow to validate the accuracy of correspondence detection (see Section 2.3.1).

2.2.2. Correspondence detection (Step 1)

For both approaches, the anatomical correspondences were established with respect to the same reference bone, selected through an iterative registration process [36]. First, we randomly selected one bone as the reference, and we registered all the other bones to the selected bone, using the Log-Demon algorithm described in the next paragraph. Then, we calculated the average transformation, and we selected the closest transformation to the average; we repeated this step until convergence. Finally, we identified the bone whose transformation was the closest to the average as the reference.

In the image-based approach, we calculated anatomical correspondences through image registration. Among all the registration algorithms available, we chose the Log-Demons because the resulting deformation vector fields (DVF) are invertible [37], which is an essential characteristic for the creation of new instances (Step 3). Invertibility comes from parameterizing DVFs with stationary velocity fields, which constitute the core of the computation. We regularized the Log-Demons with a femur-specific polyaffine model to properly capture the main anatomical features, namely the femoral head, shaft and condyles [38].

In the mesh-based approach, we computed feature correspondences using the mesh morphing algorithm developed by Boichon et al. [39]. In this algorithm, a FE volume mesh is created for the reference bone and mapped to the moving bone geometry, represented by a surface mesh. The mapping is guided by landmarks that are manually selected at corresponding anatomical features (Fig. 2). The result of the morphing is a volume mesh with the same number of elements as the reference volume mesh and with corresponding node positions. To obtain elements valid for FE simulations, node positions are regularized using the Laplacian operator. We created the surface meshes for the moving bones using the marching cube algorithm [40], and we enhanced the generated surface meshes using MRFSurface [41]. For the reference bone, we computed the volume mesh from the surface mesh using NETGEN [42]. The volume mesh was composed of approximately 125000 quadratic tetrahedrons to guarantee the mesh refinement for FE simulations [43,47]. After the morphing, we aligned the FE meshes using the Procrustes algorithm [44] to calculate the statistical appearance model.

2.2.3. Statistical appearance model (Step 2)

The statistical appearance models were computed as a combination of the statistical shape model and statistical intensity model [22] (for the complete mathematical formulation, refer to the technical report by Cootes and Taylor [45]).

The statistical shape model defines the variability of the shapes within a dataset [1]. In the image-based approach, we computed the statistical shape model as a statistical deformation model [46], calculating PCA on the stationary velocity fields from registration. In the mesh-based approach, we calculated the statistical shape model on the nodal coordinates of the FE mesh.

The statistical intensity model describes the variability of intensities within a dataset [22]. In the image-based approach, we calculated the statistical intensity model on CT images of the dataset warped to the reference bone in order to have direct correspondence among intensities. In the mesh-based approach, we computed the model on the intensity values assigned to the FE mesh nodes. For each node, we extracted the intensities from the corresponding segmented images at the node locations, and we linearly interpolated within a neighborhood of 8 voxels. For the nodes on the bone surface, we corrected the corresponding segmented images for the partial volume effect [47], which would have underestimated the mechanical properties. We eroded the outer cortical bone layer to delete the partial volume effect area, and we dilated the adjacent inner bone layer to rebuild the eroded region.

Finally, the statistical appearance model describes the combined variation of shape and intensity within the images of a dataset. The statistical shape model and the statistical intensity model are combined and weighted accordingly to their respective parameters (eigenvalues). Because of the linearity of the models, we calculated the PCA directly on the combined parameters [22].

2.2.4. Generation of new instances (Step 3)

Statistical models allow the creation of new instances within the range of variability of the original dataset [22]. Each instance is computed as a variation from the average object through a weighted linear combination of the PCA model [45]. The plausibility of the instances is assured by the variation of the parameters within a multivariate Gaussian distribution. In this study, we sampled the

parameter weights using the Latin hypercube algorithm, which covers the entire parameter space.

In the image-based approach, we assigned the new intensities to the reference bone shape, and then we warped these new intensities in the reference shape to the corresponding new bone shape using inverted DVF. In the mesh-based approach, we assigned the new intensities directly to the corresponding new node coordinates.

2.3. Validation and comparison

For each step of the pipeline, we validated the procedure of the image-based approach vs. the mesh-based approach. For calculation of statistical models and generation of new instances (Steps 2 and 3, respectively), we also compared the implications for finite element simulations. Finally, we analyzed the difference of the two approaches in terms of computational costs.

2.3.1. Correspondence detection (Step 1)

We validated the image registration and mesh morphing processes on both bone surface and bone volume. On bone surface, we calculated the Hausdorff distances between the original surface and the surface obtained after non-rigid deformation. We calculated the distance bi-directionally, and we considered the highest distance to highlight the potential failures of the correspondence detection techniques. In the bone volume, we quantified the overlap of the transformed bone to the reference bone, considering cortical tissue, cancellous tissue, and marrow. For the image-based approach, we used the Dice coefficient [48], whereas for the mesh-based pipeline, we considered the number of nodes in the regions.

2.3.2. Statistical appearance model and FE simulations (Step 2)

We evaluated the statistical appearance models using the three criteria recommended by Davis et al. [49]: compactness, representation and generalization. Compactness evaluates the ability of the model at describing the dataset with the fewest number of parameters, and it is calculated as the accumulation of the normalized PCA variance. Representation is the capacity of the model to recreate objects that are part of the training dataset. Generalization is the ability of the model at generating instances that are not part of the original dataset. Therefore, we recreated 25 femurs randomly selected from the original dataset to test the model representation, and 25 bones were excluded from the original dataset to evaluate the model generalization. For each of the three metrics, shapes and intensities of femurs were generated starting from the first mode (i.e. PCA eigenvector) and adding 10 modes for each recalculation, until the total amount of modes was reached.

To evaluate the implication of statistical appearance models on FE simulations, we compared the FE results of bones reconstructed for representation and generalization against the FE results of the corresponding bones in the original dataset. In previous studies, where authors analyzed ability of mesh-based models at predicting mechanical behavior, original bones were conceived as the volumetric meshes used to calculate PCA [29,30]. In image-based approaches, original bone shape could be represented by deformation fields, and original bone intensities can be conceived as the intensities warped to the reference, because deformation fields and warped intensities are used to calculate PCA. In our study it would be impossible to compare FE results from the two approaches using the previous criteria, because original bones are represented differently in the two cases, i.e. as meshes and images. To have unique original bones to compare with our FE results, we chose to use the original segmented CT images. As reconstructed bones, we used instances generated by the two models utilizing all the modes, both for the image-based approach and the mesh-based approach. For the original bones and the image-based reconstructed bones, we created FE meshes with a process similar to the creation of the reference bone in mesh morphing: we extracted the bone surface with the marching cube algorithm, enhanced the mesh with MRFSurface and created the volumetric mesh with NETGEN. For mesh-based reconstructed bones, FE meshes were already available as the result of mesh morphing. As for the reference bone, volume meshes were composed of approximately 125,000 quadratic tetrahedrons, to fulfil the criteria from literature [43,47] (average number of mesh elements: 125,924; average edge length: 3.5 mm). For each bone, we defined physiological boundary conditions as proposed by Speirs et al. [51], and we applied a force of 1000 N, directed from the femoral head to the intercondyle region [50] (Fig. 3(a)). Forces and boundary conditions were applied at corresponding anatomical positions, which were detected through DVF for the image-based bones and through node correspondence for the mesh-based bones. We calculated material properties from image intensities, as proposed by Schileo et al. [24] (Fig. 3(b)). We performed a linear pseudo-calibration to account for non-calibrated images. We converted image intensities to bone ash density (range from 0.10 g/cm^3 to 1.08 g/cm^3 [23]), and then converted ash density to apparent density using a ratio of 0.60 to include the organic part of the bone [52,53]. Finally, we calculated the Young's modulus using the femur-specific equation proposed by Morgan et al. [54]: $E = 6.850\rho_{app}{}^{1.49}$, where ρ_{app} is the apparent density. On the bone surface, we corrected the partial volume effect using the same procedure described in Section 2.2.3. We assumed a Poisson ratio of 0.3 [55]. The simulations were run in Abaqus 6.10 (Simulia, Providence, USA), solving at nodes where the Young's modulus was associated to temperature through a linear relationship [47]. To evaluate model performances in FE, we compared nodal principal strains of the original bones against nodal principal strains of bones reconstructed with the two models. For each bone, we interpolated the principal strains of the reconstructed bone at the nodes of the original bone, and we analyzed their correlation. In addition, we compared maximum principal strains at the femoral neck (Fig. 3(c)). On the reference bone, we manually selected two points (Fig. 3(c) (top)), and then we propagated the two points to each bone. For the original bones and the bones reconstructed with the image-based approach, we propagated the two points using deformation vector fields; for the bones reconstructed with the mesh-based approach, we mapped the two points through mesh correspondence. For each bone, we averaged strains from 4 concentric rings of elements extracted from the two points in the femoral neck (Fig. 3(c) (bottom)).

2.3.3. Generation of new instances (Step 3)

The plausibility of the instances generated with the two approaches was guaranteed statistically by the Gaussian distribution of the parameters [22]. Thus, we evaluated the new instances only in terms of quality of the FE meshes. For the image-based approach, we transformed the created images to FE meshes with the procedure used to mesh the reference bone for the morphing (see Section 2.2.2). For the mesh-based approach, the new instances were created as volumetric meshes directly suitable for the evaluation. We analyzed the quality of the mesh elements using three criteria: Jacobian, edge ratio and minimum angle. The Jacobian is a measure of volume. When negative, it represents a strongly distorted element, inappropriate for finite element calculations, whereas when positive, the Jacobian guarantees element suitability for FE calculations. The edge ratio is a measure of size, and it was computed as the ratio between the longest and the shortest edge of each element. Finally, the minimum angle is a measure of shape, and it was calculated as the smallest angle between two sides of each element.

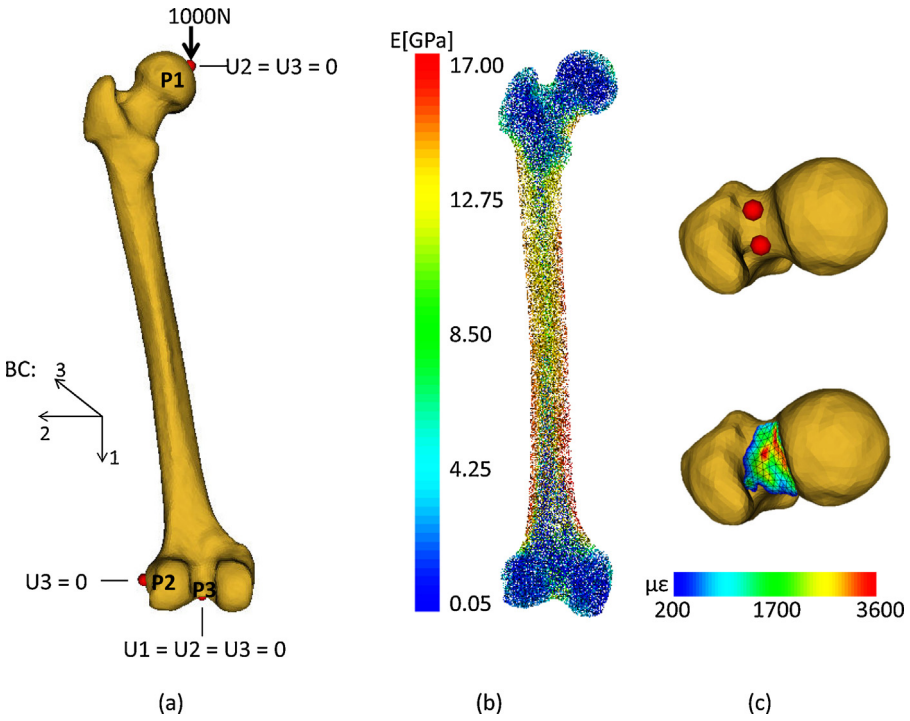

Fig. 3. Boundary conditions, distribution of mechanical properties for FE simulations and calculation of neck strains. (a) Boundary conditions. In the femoral head, the node P1 was constrained in two translational degrees of freedom (DOFs) to allow deflection toward the center of the knee. In the lateral epicondyle, the node P2 was constrained with one DOF to prevent the rotation of the bone around its axis. In the intercondyle area, the node P3 was constrained in three DOFs to represent the knee joint. (b) Assignment of mechanical properties to mesh nodes. The partial volume effect was corrected in the periosteal region of the cortical bone. (c) Calculation of strains at the femoral neck. The two points propagated to each bone and used to define the volume of interest (top) and map of strains in the neck region (bottom).

3. Results

3.1. Correspondence detection (Step 1)

The mesh-based approach performed better on the bone surface, with an average Hausdorff distance less than 3 mm, about the half of the distance for the image-based approach (about 5.1 ± 1.17 mm) (Table 1(a)). The image-based approach had better results in the bone volume, where the amount of volume overlap was from 10% to 20% better than for the mesh-based approach (Table 1(b)).

3.2. Statistical appearance models and FEM simulations (Step 2)

The statistical appearance model generated with the mesh-based approach had a greater compactness than the model created with the image-based approach (Fig. 4(a)). The compactness difference spanned from 6% to 15% in the first 60 modes, before converging. For the representation, the mesh-based approach had better performance when recreating bone shapes, whereas the image-based approach had better results at reconstructing original intensities (Fig. 4(b)). At the first mode, the reconstruction error for shapes was less than 2 mm for the mesh-based model and more than 5 mm for the image-based model, whereas for intensities the error was 7% for the mesh-based approach and 0.3% for the image-based approach. For the generalization, the two approaches performed similarly to the representation (Fig. 4(c)). In both cases, they reached a plateau of performances at mode 40, where the reconstruction error for shapes was about 1 mm for the mesh-based model and less than 2 mm for the image-based model. The error was 4% (80 HU) for the intensities with the mesh-based model, while the image-based model had a constant low error of 0.3% (6 HU).

In FE simulations, the image-based approach showed better performance than the mesh-based approach. A total of 14 meshes from the representation and 2 meshes from the generalization created with the mesh-based approach had 1 to 4 elements with a null or negative Jacobian, therefore they could not be used for FE calculations (Table 3). The image-based and the mesh-based approaches predicted similar principal strains of original bones (Fig. 5). Values of R^2 were slightly higher for the image-based method ($\max R^2 = 0.98$, $\min R^2 = 0.92$) than for the mesh-based

Table 1
Evaluation of correspondence detection (a) on bone surface and (b) in bone volume.

(a)

Surface Metric	Image-based approach	Mesh-based approach
Hausdorff distance [mm]	5.10 ± 1.17	2.71 ± 1.21

(b)

Volume metrics	Image-based approach	Mesh-based approach
Cortical bone overlapping [%]	85.42 ± 7.90	65.67 ± 6.02
Trabecular bone overlapping [%]	85.64 ± 9.14	73.29 ± 11.15
Marrow overlapping [%]	79.24 ± 10.34	75.29 ± 15.11

Table 2
Computational costs for the calculation of the statistical models and the creation of one new instance. In the image-based approach, the time for computing a new instance refers to both the creation of a new image and the transformation to a FE mesh.

Process	Image-based approach	Mesh-based approach
Shape PCA	4.2 h[a]	11 min[b]
Intensity PCA	1.2 h[a]	2 min[b]
Combined PCA	5 h[b]	1 min[b]
New instance	6 min[b]	10 s[b]

[a] Processor: Intel Xeon CPU, X5550@2.67 GHz. RAM: 48 GB.
[b] Processor: Intel Core Duo, E8500@3.16 GHz. RAM: 8 GB.

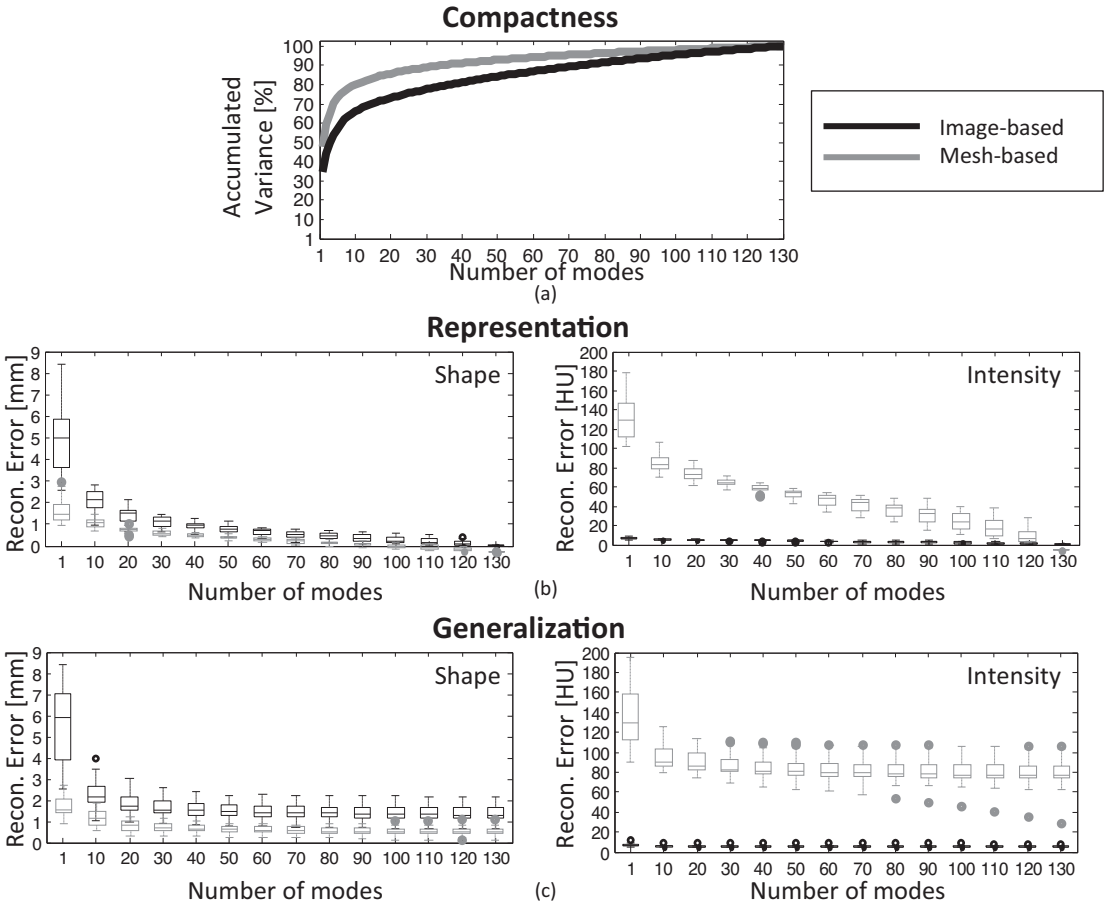

Fig. 4. Validation of the statistical appearance models generated with the image-based and the mesh-based approaches: (a) compactness, (b) representation and (c) generalization. Circles represent outliers.

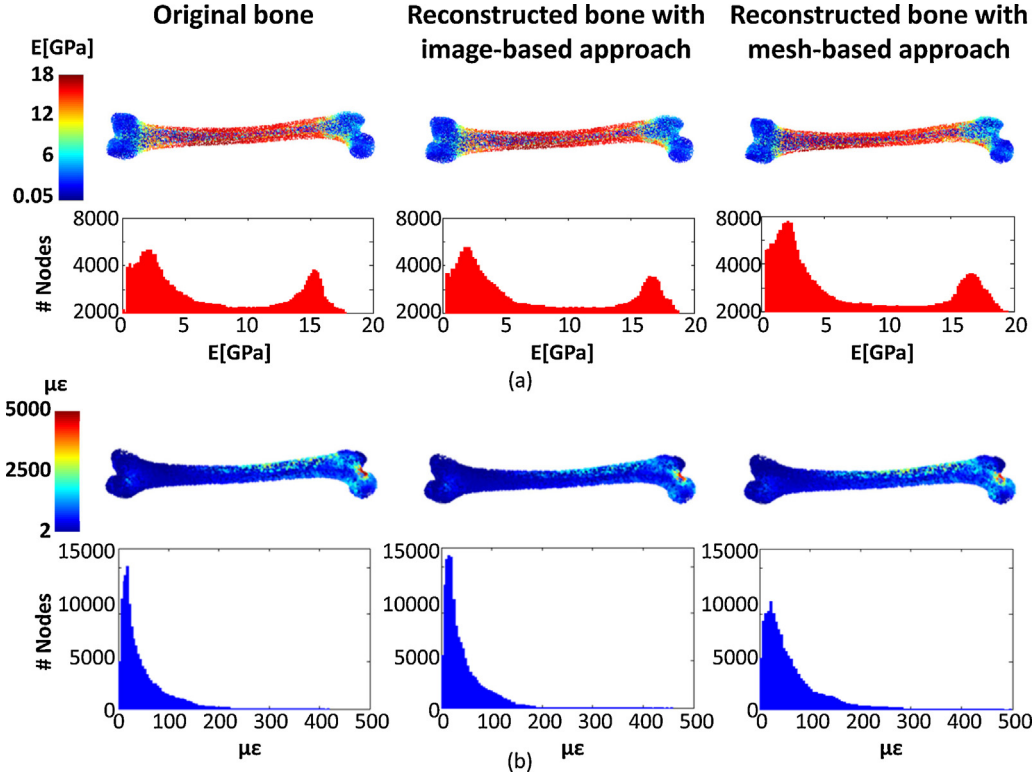

Fig. 5. Representative case of mechanical behavior for original bone, bone recreated with image-based approach and bone reconstructed with mesh-based approach. Mechanical properties (a) and maximum principal strain (b) visualized at mesh nodes and as a histogram for the three bones.

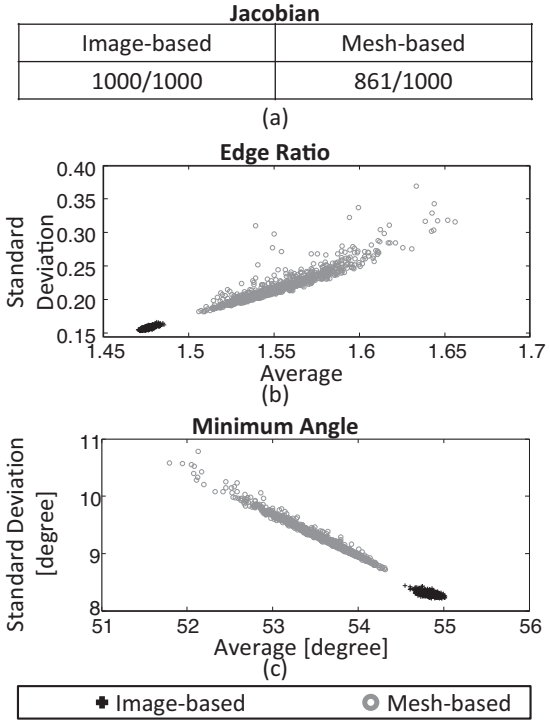

Fig. 6. Evaluation of the quality of the FE meshes generated from the statistical appearance models: (a) Jacobian, (b) edge ratio and (c) minimum angle.

method ($\max R^2 = 0.92$, $\min R^2 = 0.84$), both for the representation dataset (Table 3(a)) and the generalization dataset (Table 3(b)).

3.3. Generation of new instances and mesh quality (Step 3)

For both approaches, we created 1000 new instances that covered 90% of the variation. The new bones were generated using 73 modes for the image-based approach and using 34 modes for the mesh-based approach. All of the meshes generated with the image-based approach had elements with positive Jacobian values, whereas 139 meshes from the mesh-bases approach had elements with a null or negative Jacobian (Fig. 6(a)). The elements of the FE meshes from the image-based model had a more homogeneous edge ratio than the FE meshes from the mesh-based model, both in terms of mean and standard deviation (Fig. 6(b)). A similar behavior was observed for the minimum angle (Fig. 6(c)).

3.4. Computational costs

In the image-based approach, the model was computed in the order of hours, whereas in the mesh-based approach, the model was created in the order of minutes. The creation of the new instances required minutes for the image-based approach, whereas it required seconds for the mesh-based approach (Table 2).

4. Discussion

In this study, we compared an image-based and a mesh-based approach to create statistical appearance models of the femur for mechanical simulations. The accuracy of correspondence detection was higher for bone volume using the image-based approach and it was higher for bone surface using the mesh-based approach. The image-based approach reproduced intensities more accurately, whereas the mesh-based approach reproduced shapes more accurately. In FE simulations, strains were predicted similarly for the two approaches, and the mesh-based approach failed at creating valid FE meshes for all instances.

Detection of anatomical landmarks constitutes the main challenge when building statistical models. In this study, we used polyaffine diffeomorphic demons for image registration [38] and a landmark-based approach for mesh morphing [39]. These two algorithms represent the state of the art in the respective fields due to their high computational efficiency and their available implementations for the femur. To create valid correspondences for statistical models, the two algorithms must fulfill specific constraints. The image registration algorithm has to be diffeomorphic, as it must produce deformation vector fields that are invertible for the creation of new instances. The mesh morphing algorithm has to guarantee the creation of meshes that are valid for FE simulations, while keeping accurate anatomical correspondences. Our findings reflected the intrinsic properties of each algorithm. The mesh morphing was initialized by surface landmarks, and the surface mesh was back-projected to the target geometry at each iteration for shape accuracy. Moreover, the internal node position required smoothing to create high quality elements, compromising correspondence accuracy. Image registration was based on correspondences among grey levels and had no constraints related to the element quality or the object geometry. The evaluation of bone correspondences was global. On the bone surface, the calculation of correspondence accuracy was limited by the small amount of anatomical features that were easily identifiable. In the bone volume, no precise morphological structures could be identified.

Performances of the statistical appearance models were a direct consequence of the correspondence detection algorithms and the characteristics of the models. The compactness of the statistical appearance model was higher for the mesh-based approach, probably because the smoothing of node coordinates for element quality decreased the variability described by the model. In both representation and generalization, the mesh-based model performed better at recreating shapes because of the high accuracy of the mesh morphing on the mesh surface. The image-based model performed better at reproducing intensities, since it was not constrained by the trade-off between element quality and correspondence accuracy. The quality of the meshes created as new instances was higher for the image-based approach, as meshes were created individually. All of the elements had a positive Jacobian, similar edge ratio and minimum angle, therefore they could be directly used for FE simulations, although direct comparison of the results would be limited. For the mesh-based approach, more than 10% had null or negative Jacobian, and elements had very diverse edge ratio and minimum angle, compromising the use for FE simulations in population studies.

Implications of the two statistical appearance models on FE results and FE mesh quality were determined by the intrinsic characteristics of the models and data processing. For both approaches, we compared FE results of reconstructed bones to FE results of common original bones. In contrast to previous studies [29,30], we chose the original subjects' CT datasets as original bones, instead of images or meshes used to calculate PCA. This choice was made in order to compare both models to the same dataset. As a consequence, strains from reconstructed bones did not fully predict strains from the original bones. The reason for this discrepancy might reside in interpolation. To build the image-based model, intensities of the image dataset are warped to the reference bone shape, where PCA is calculated. To create new instances, intensities are first assigned from the PCA to the reference bone shape, and then warped to their corresponding new shape. Therefore, to reconstruct a subject's image, two warping processes must occur, and thus two interpolations. In the mesh-based method, intensities associated to meshes result from image interpolation at the mesh nodes. New instances are created as meshes, where the intensities

Table 3
Comparison of principal strains of original bone against bones recreated with an image-based approach and a mesh-based approach for (a) the representation dataset and (b) the generalization datasets. Mean values and maximum values refer to maximum principal strains ($\mu\varepsilon$). Values of R^2 represent the quality of regression for minimum and maximum principal strains for each method against the original bones. Missing values correspond to an invalid FE mesh created by the mesh-based approach.

(a)

Representation dataset

No. bone	1	2	3	4	5	6	7	8	9	10	11	12	13	14	15	16	17	18	19	20	21	22	23	24	25
Mean strain ($\mu\varepsilon$)																									
Original	417	437	460	470	428	495	537	278	507	531	548	390	488	322	587	454	390	420	448	384	465	418	576	445	398
Image-based	401	387	432	448	464	449	600	247	522	546	495	371	497	348	573	456	350	464	432	377	476	379	556	489	357
Mesh-based			614		534		668	302	629		572	483			689		419			442					479
Max strain ($\mu\varepsilon$)																									
Original	3621	4562	4192	5113	5315	5584	7915	3023	5774	5898	5599	4567	4614	2932	5415	5033	3496	4131	4687	4205	5310	4842	5755	5422	3619
Image-based	4386	3708	4592	5566	6649	4464	6773	2436	6660	8266	3381	5371	4611	3733	8580	6649	3268	4518	5275	4186	5679	3289	5854	6352	3392
Mesh-based			4992		4705		7919	3049	7068		3086	7486			7879		3775			4550					4523
R^2																									
Image-based	0.98	0.97	0.97	0.98	0.96	0.96	0.98	0.95	0.97	0.95	0.96	0.97	0.96	0.97	0.92	0.93	0.96	0.94	0.97	0.95	0.95	0.96	0.93	0.93	0.97
Mesh-based			0.92		0.94		0.91	0.94	0.95		0.92	0.87			0.84		0.95			0.95					0.92
Neck strain mean ($\mu\varepsilon$)																									
Original	1196	1310	1322	1655	1371	1592	1816	715	1605	1608	1612	1135	1338	932	1348	1439	1013	1227	1244	1202	1375	1289	1800	1396	1278
Image-based	1310	1166	1244	1686	1921	1378	2023	730	1757	1848	1462	1266	1539	1045	1681	1653	1031	1570	1474	1383	1695	1022	1739	1711	1118
Mesh-based			1599		1942		2203	826	2169		1587	1544			2336		1280			1443					1378

(b)

Generalization dataset

No. bone	1	2	3	4	5	6	7	8	9	10	11	12	13	14	15	16	17	18	19	20	21	22	23	24	25
Mean strain ($\mu\varepsilon$)																									
Original	404	357	579	458	438	329	453	396	402	421	378	516	401	397	465	417	386	437	370	422	541	352	274	420	317
Image-based	425	383	529	422	425	300	439	405	394	345	391	474	455	447	475	394	398	437	349	437	585	360	310	391	291
Mesh-based	513	373	670	567	492	369	542	516	508	431	473	489	541	565	595	512	434	540	418			431	391	524	375
Max strain ($\mu\varepsilon$)																									
Original	4910	4894	7414	4831	4115	2786	5717	4773	4060	4100	4517	6341	4687	4898	5371	4474	4259	4974	4443	4558	7540	3525	3553	4598	4083
Image-based	3203	3736	5168	4635	4524	3200	5271	4820	3556	3750	4582	5260	4063	5558	4453	3978	3545	5529	3279	4668	5725	3889	2992	4567	2946
Mesh-based	3446	3161	7175	5920	4033	4052	6013	6174	5115	3752	4677	3978	3871	4380	8603	4753	3524	6437	2973			5027	4141	6010	3475
R^2																									
Image-based	0.97	0.95	0.92	0.95	0.95	0.95	0.96	0.97	0.96	0.94	0.94	0.97	0.93	0.94	0.94	0.97	0.97	0.96	0.95	0.96	0.94	0.94	0.94	0.96	0.94
Mesh-based	0.89	0.93	0.92	0.95	0.93	0.92	0.93	0.96	0.96	0.93	0.95	0.87	0.93	0.93	0.93	0.92	0.91	0.91	0.89			0.91	0.92	0.96	0.91
Neck mean strain ($\mu\varepsilon$)																									
Original	1399	1096	1793	1409	1136	849	1461	1197	1131	1141	1169	1908	1222	1086	1661	1323	1138	1207	1151	1317	1701	1051	757	1177	1049
Image-based	1426	1298	1726	1309	1534	1102	1510	1378	1159	1083	1271	1629	1543	1482	1804	1294	1187	1418	1234	1628	2032	1259	830	1209	1029
Mesh-based	1735	944	2083	1740	1464	1258	1854	1743	1516	1206	1562	1555	1937	1816	2170	1363	1316	1749	1326			1413	1146	1648	1156

do not represent the full information contained in the patients' CT images. Also in this case, interpolation is present in the process. Interpolation can cause high intensity differences, especially in transition areas between cortical bone, cancellous bone and bone marrow: a difference of 50 Hounsfield Units translate to a difference of $E = 1.13$ GPa (from conversions used in this study). Interpolation should be taken into account when evaluating strain prediction against the original subjects' CT images in patient-specific applications. Statistical appearance models could be a valid approach to predict patient-specific mechanical behavior of bones from CT Images [56]: given a model of shape and intensities and predicted strains, it would be possible to predict strains for any new subject's CT image.

Finally, the two approaches showed remarkable differences in terms of computational costs. The calculation of the model and the creation of new instances required lower memory and time for the mesh-based approach than for the image-based approach. Costs to create the model can be critical for applications involving optimization procedures or real time prediction, but they are negligible when compared to FE simulation costs.

To date, few studies have been proposed that combine statistical appearance models and FE simulation for femurs. Bryan et al. [7,30] used a mesh-based approach to predict fracture risk within a population. Data are not suitable to compare morphing results, but model compactness and representation were close to our study. Similarly, Nicolella et al. [29] created a mesh-based approach to parameterize shape and mechanical properties of the femur. The mesh-morphing algorithm had higher accuracy than ours on bone surface. Comparison in bone volume is not possible as they considered bone density whereas we evaluated CT intensities. Finally, Schuler et al. [9] created an image-based statistical appearance model to assess fracture risk. They used diffeomorphic demons to ensure the DVF invertibility, but they did not investigate the creation and quality of FE meshes, therefore no comparison could be investigated.

The present work has limitations that must be addressed. First, in this study we used algorithms that are considered state of the art for registration and mesh morphing. We are aware that different algorithms could be used for the same purpose and could potentially lead to different results. However, we believe that the use of other algorithms would not compromise the conceptual findings of this study. Invertibility for registration and compromise between correspondence accuracy and element quality for mesh morphing are unavoidable constraints. Second, the images we used to create the models lacked calibrated CT intensity, which is a fundamental requirement for FE simulation. We addressed this limitation by performing a pseudo-calibration.

The use of statistical models in biomechanics is relatively new and there are many possibilities for its applications. Statistical shape models are currently used to study bone geometry, and could be used in biomechanics to investigate the impact of shape on mechanical behavior for a fixed Young's modulus. Statistical intensity models could be used to investigate the impact of different material properties given a fixed bone shape. Statistical appearance models could be useful to study the impact of combined variation of shape and Young's modulus in bone mechanical behavior, as has been done for prediction of bone strength [28,29] and fracture risk [9,30]. These models have great potential to investigate bone mechanical behavior in synthetic populations. However, when applied to patient–specific prediction of mechanical behavior, model accuracy should be taken into account. In this study, we found that the image-based approach is more accurate in volume correspondence detection, recreation of FE displacements and quality of FE mesh, whereas the mesh-based approach is more accurate in surface correspondence detection, model compactness, and creation of meshes with corresponding elements. Therefore, based on our results, we recommend the use of image-based statistical appearance model for FE simulations of the femur, as it calculates more accurate mechanical properties and it creates valid FE meshes.

Funding

The work was partially funded by Swiss National Science Foundation through the NCCR Co-Me.

Ethical approval

Data acquisition was fully anonymized and controlled by a governmental data protection agency (DatenschutzbeauftragterStadt Bremen, Bremen, Germany).

Supplementary material

Data are available at The Virtual Skeleton Database (www.virtualskeleton.ch); code is available upon request to the first author.

Acknowledgement

This work was supported by the Swiss National Center of Competences in Research (NCCR) Co-Me. The authors deeply thank Dr. Benedikt Helgason for his help with the assignment of mechanical properties from CT images, and the reviewers for providing constructive inputs to our manuscript.

Conflict of interest statement

All authors have no conflict of interest.

References

[1] Cootes T, Taylor C, Cooper D, Graham J. Active shape models—their training and application. Comput Vision Image Understanding 1995;61(1):38–59.
[2] Lamecker H, Lange T, Seebass M. A statistical shape model for the liver. In: Medical image computing and computer-assisted intervention—MICCAI 2002. 2002. p. 421–7.
[3] Styner M, Gerig G, Lieberman J, Jones D, Weinberger D. Statistical shape analysis of neuroanatomical structures based on medial models. Med Image Anal 2003;7(3):207–20.
[4] Lötjönen J, Kivistö S, Koikkalainen J, Smutek D, Lauerma K. Statistical shape model of atria, ventricles and epicardium from short- and longaxis MR images. Med Image Anal 2004;8(3):371–86.
[5] Paulsen RR, Nielsen C, Laugesen S, Larsen R. Using a shape model in the design of hearing aids. SPIE—Med Imaging 2004;5370:1304–11.
[6] Baldwin MA, Langenderfer JE, Rullkoetter PJ, Laz PJ. Development of subject-specific and statistical shape models of the knee using an efficient segmentation and mesh-morphing approach. Comput Methods Programs Biomed 2010;97(3):232–40.
[7] Bryan R, Nair PB, Taylor M. Use of a statistical model of the whole femur in a large scale, multi-model study of femoral neck fracture risk. J Biomech 2009;42(13):2171–6.
[8] Bredbenner TL, Eliason TD, Potter RS, Mason RL, Havill LM, Nicolella DP. Statistical shape modeling describes variation in tibia and femur surface geometry between control and incidence groups from the osteoarthritis initiative database. J Biomech 2010;43(9):1780–6.
[9] Schuler B, Fritscher KD, Kuhn V, Eckstein F, Link TM, Schubert R. Assessment of the individual fracture risk of the proximal femur by using statistical appearance models. Med Phys 2010;37(6):2560–71.
[10] Fritscher KD, Grünerbl A, Schubert R. 3D image segmentation using combined shape-intensity prior models. Int J Comput Assisted Radiol Surg 2007;1(6):341–50.
[11] Schmid J, Magnenat-Thalmann N. MRI bone segmentation using deformable models and shape priors. In: Medical image computing and computer-assisted intervention—MICCAI 2008. 2008. p. 562–9.
[12] Yao J, Taylor R. Assessing accuracy factors in deformable 2D/3D medical image registration using a statistical pelvis model. In: Proceeding of the ninth IEEE international conference on computer vision—ICCV 2003, vol. 2. 2003. p. 1329–34.

[13] Benameur S. 3D/2D registration and segmentation of scoliotic vertebrae using statistical models. Comput Med Imaging Graph 2003;27(5):321–37.
[14] Deligianni F, Chung A, Yang GZ. Nonrigid 2-D/3-D registration for patient specific bronchoscopy simulation with statistical shape modeling: phantom validation. IEEE Trans Med Imaging 2006;25(11):1462–71.
[15] Zheng G, Gollmer S, Schumann S, Dong X, Feilkas T, Gonzalez Ballester MA. A 2D/3D correspondence building method for reconstruction of a patient-specific 3D bone surface model using point distribution models and calibrated X-ray images. Med Image Anal 2009;13(6):883–99.
[16] Blanz V, Mehl A, Vetter T, Seidel HP. A statistical method for robust 3D surface reconstruction from sparse data. In: Second International Symposium on 3D Data Processing, Visualization and Transmission—3DPVT'04. 2004.
[17] Rajamani KT, Styner M, Talib H, Zheng G, Nolte LP, Gonzalez Ballester MA. Statistical deformable bone models for robust 3D surface extrapolation from sparse data. Med Image Anal 2007;11(2):99–109.
[18] Rao A, Aljabar P, Rueckert D. Hierarchical statistical shape analysis and prediction of sub-cortical brain structures. Med Image Anal 2008;12(1):55–68.
[19] Blanc R, Reyes M, Seiler C, Szekely G. Conditional variability of statistical shape models based on surrogate variables. In: Medical image computing and computer-assisted intervention: MICCAI international conference on medical image computing and computer-assiste Intervention, 12(Pt 2). 2009. p. 84–91.
[20] Zheng G. Statistical shape model-based reconstruction of a scaled, patient-specific surface model of the pelvis from a single standard AP x-ray radiograph. Med Phys 2010;37:1424–39.
[21] Hotelling H. Analysis of a complex of statistical variables into principal components. J Educ Psychol 1933;24(6):417–41.
[22] Cootes TF, Taylor CJ. Statistical models of appearance for medical image analysis and computer vision. SPIE Med Imaging SPIE 2001;4322:236–48.
[23] Keyak JH, Meagher JM, Skinner HB, Mote CD. Automated three-dimensional finite element modelling of bone: a new method. J Biomed Eng 1990;12(5):389–97.
[24] Schileo E, Dall'Ara E, Taddei F, Malandrino A, Schotkamp T, Baleani M, et al. An accurate estimation of bone density improves the accuracy of subject-specific finite element models. J Biomech 2008;41(11):2483–91.
[25] Helgason B, Perilli E, Schileo E, Taddei F, Brynjolfsson S, Viceconti M. Mathematical relationships between bone density and mechanical properties: a literature review. Clin Biomech 2008;23(2):135–46.
[26] Ciarelli MJ, Goldstein SA, Kuhn JL, Cody DD, Brown MB. Evaluation of orthogonal mechanical properties and density of human trabecular bone from the major metaphyseal regions with materials testing and computed tomography. J Orthop Res 1991;9(5):674–82.
[27] Taddei F, Pancanti A, Viceconti M. An improved method for the automatic mapping of computed tomography numbers onto finite element models. Med Eng Phys 2004;26(1):61–9.
[28] Querol L, Büchler P, Rueckert D, Nolte L. Statistical finite element model for bone shape and biomechanical properties. In: Medical image computing and computer-assisted intervention—MICCAI 2006. 2006. p. 405–11.
[29] Nicolella DP, Bredbenner TL. Development of a parametric finite element model of the proximal femur using statistical shape and density modelling. Comput Methods Biomech Biomed Eng 2012;15(2):101–10.
[30] Bryan R, Mohan PS, Hopkins A, Galloway F, Taylor M, Nair PB. Statistical modelling of the whole human femur incorporating geometric and material properties. Med Eng Phys 2010;32(1):57–65.
[31] Whitmarsh T, Fritscher KD, Humbert L, Del Rio Barquero LM, Roth T, Kammerlander C, et al. A statistical model of shape and bone mineral density distribution of the proximal femur for fracture risk assessment. In: Medical image computing and computer-assisted intervention: MICCAI international conference on medical image computing and computer-assisted intervention, 14(Pt 2). 2011. p. 393–400.
[32] Rueckert D, Sonoda LI, Hayes C, Hill DL, Leach MO, Hawkes DJ. Nonrigid registration using free-form deformations: application to breast MR images. IEEE Trans Med Imaging 1999;18(8):712–21.
[33] Vercauteren T, Pennec X, Perchant A, Ayache N. Symmetric log-domain diffeomorphic registration: a demons-based approach. In: Medical image computing and computer-assisted intervention—MICCAI 2008, 11. 2008. p. 754–61.
[34] Hraiech N. Mesh morphing and shape indexing in human femur modeling applications. Rennes: Universite de Rennes; 2010 (Ph.D. thesis).
[35] Grassi L, Hraiech N, Schileo E, Ansaloni M, Rochette M, Viceconti M. Evaluation of the generality and accuracy of a new mesh morphing procedure for the human femur. Med Eng Phys 2011;33(1):112–20.
[36] Guimond A, Meunier J, Thirion JP. Average brain models: a convergence study. Comput Vision Image Understanding 2000;77(2):192–210.
[37] Vercauteren T, Pennec X, Perchant A, Ayache N. Diffeomorphic demons: efficient non-parametric image registration. NeuroImage 2009;45(1 Suppl):S61–72.
[38] Seiler C, Pennec X, Reyes M. Capturing the multiscale anatomical shape variability with polyaffne transformation trees. Med Image Anal 2012;16(7):1371–84.
[39] Boichon C, Rochette M, Schileo E, Grassi L, Taddei F, Viceconti M. Shape indexing of human femora using morphing and principal component analysis. In: First virtual physiological human conference—VPH2010, 1. 2011.
[40] Lorensen WE, Cline HE. Marching cubes: a high resolution 3D surface construction algorithm. Comput Graphics 1987;21(4):163–9.
[41] Paulsen RR, Baerentzen JA, Larsen R. Markov random field surface reconstruction. IEEE Trans Visual Comput Graphics 2010;16(4):636–46.
[42] Schöberl J. NETGEN: an advancing front 2D/3D-mesh generator based on abstract rules. Comput Visual Sci 1997;1:41–52.
[43] Viceconti M, Davinelli M, Taddei F, Cappello A. Automatic generation of accurate subject-specific bone finite element models to be used in clinical studies. J Biomech 2004;37(10):1597–605.
[44] Goodall C. Procrustes methods in the statistical analysis of shape. J R Stat Soc Ser B: Methodological 1991;53(2):285–339.
[45] Cootes T, Taylor C. Statistical model of appearance for computer vision. In: Tech. Rep.; imaging science and biomedical engineering. Manchester: University of Manchester; 2004.
[46] Rueckert D, Frangi AF, Schnabel J. Automatic construction of 3-D statistical deformation models of the brain using nonrigid registration. IEEE Trans Med Imaging 2003;22(8):1014–25.
[47] Helgason B, Taddei F, Palsson H, Schileo E, Cristofolini L, Viceconti M, et al. A modified method for assigning material properties to FE models of bones. Med Eng Phys 2008;30(4):444–53.
[48] Tustison NJ, Gee JC. Introducing dice, jaccard, and other label overlap measures to ITK. Insight J 2009.
[49] Davies R, Twining C, Taylor C. Statistical models of shape: optimization and evaluation. London: Springer; 2008.
[50] Keyak JH, Rossi Sa, Jones Ka, Skinner HB. Prediction of femoral fracture load using automated finite element modeling. J Biomech 1998;31(2):125–33.
[51] Speirs AD, Heller MO, Duda GN, Taylor WR. Physiologically based boundary conditions in finite element modelling. J Biomech 2007;40(10):2318–23.
[52] Goulet RW, Goldstein Sa Ciarelli MJ, Kuhn JL, Brown MB, Feldkamp LA. The relationship between the structural and orthogonal compressive properties of trabecular bone. J Biomech 1994;27(4):375–89.
[53] Keyak JH, Lee IY, Skinner HB. Correlations between orthogonal mechanical properties and density of trabecular bone: use of different densitometric measures. J Biomed Mater Res 1994;28:1329–39.
[54] Morgan E, Bayraktar H, Keaveny T. Trabecular bone modulus–density relationships depend on anatomic site. J Biomech 2003;36(7):897–904.
[55] Wirtz DC, Schiers N, Pandorf T, Radermacher K, Weichert D, Forst R. Critical evaluation of known bone material properties to realize anisotropic FE-simulation of the proximal femur. J Biomech 2000;33(10):1325–30.
[56] Blanc R, Seiler C, Székely G, Nolte L-P, Reyes M. Statistical model based shape prediction from a combination of direct observations and various surrogates: application to orthopaedic research. Med Image Anal 2012;16(6):1156–66.